Measurement of the decay of laser-driven linear plasma wakefields

J. Jonnerby,[1,*] A. von Boetticher,[1] J. Holloway,[1] L. Corner,[2] A. Picksley,[1,†] A. J. Ross,[1] R. J. Shalloo,[3,‡] C. Thornton,[4] N. Bourgeois,[4] R. Walczak,[1,§] and S. M. Hooker[1,‖]

[1]*John Adams Institute for Accelerator Science and Department of Physics, University of Oxford, Denys Wilkinson Building, Keble Road, Oxford OX1 3RH, United Kingdom*

[2]*Cockcroft Institute of Accelerator Science, University of Liverpool, Liverpool WA4 4AD, United Kingdom*

[3]*John Adams Institute for Accelerator Science, Imperial College London, London SW7 2AZ, United Kingdom*

[4]*Central Laser Facility, STFC Rutherford Appleton Laboratory, Didcot OX11 0QX, United Kingdom*

(Received 20 June 2023; accepted 10 October 2023; published 27 November 2023)

We present measurements of the temporal decay rate of one-dimensional (1D), linear Langmuir waves excited by an ultrashort laser pulse. Langmuir waves with relative amplitudes of approximately 6% were driven by 1.7 J, 50 fs laser pulses in hydrogen and deuterium plasmas of density $n_{e0} = 8.4\times10^{17}\,\mathrm{cm}^{-3}$. The wakefield lifetimes were measured to be $\tau_{\mathrm{wf}}^{\mathrm{H}_2} = (9\pm2)$ ps and $\tau_{\mathrm{wf}}^{\mathrm{D}_2} = (16\pm8)$ ps, respectively, for hydrogen and deuterium. The experimental results were found to be in good agreement with 2D particle-in-cell simulations. In addition to being of fundamental interest, these results are particularly relevant to the development of laser wakefield accelerators and wakefield acceleration schemes using multiple pulses, such as multipulse laser wakefield accelerators.

DOI: 10.1103/PhysRevE.108.055211

I. INTRODUCTION

Next-generation plasma wakefield particle accelerators use charged beams or laser pulses to excite Langmuir waves that can support accelerating gradients on the order of GeV/cm [1]. Considerable progress has been made in this sphere in recent years, including, for example: the acceleration to multi-GeV-scale energies in wakefields driven by laser pulses [2,3], electron bunches [4,5], and by long proton bunches [6]; and applications of plasma-accelerated beams to the generation of radiation [7], and the first demonstrations of gain in free-electron-laser experiments [8,9].

In the original concept [1] of a laser-driven plasma accelerator, the driving laser pulse had a duration shorter than the plasma period $T_{\mathrm{pe}} = 2\pi/\omega_{\mathrm{pe}}$, where $\omega_{\mathrm{pe}} = (n_{e0}e^2/m_e\epsilon_0)^{1/2}$, and in which e is the electron charge, m_e is the electron mass, and ϵ_0 is the vacuum permittivity. Many important results have been obtained in this regime, for both laser- and particle-beam-driven plasma accelerators, and this regime continues to be a major focus of research worldwide. However, it is also possible to drive the plasma wakefield with: (i) a train of short drive pulses, spaced by T_{pe}; or (ii) by a drive pulse that is long compared to T_{pe}, but with a temporal intensity profile that is modulated with a period of T_{pe} [4,6,10–12].

We recently extended this latter concept by proposing a method [13] for generating the required pulse train: frequency modulation of a long laser pulse by a plasma wave driven by a short, low-energy seed pulse, followed by temporal compression in a dispersive optical system. Simulations of this scheme show that electrons could be accelerated to 0.65 GeV in a plasma stage driven by a pulse train generated by a 1.7 J, 1 ps drive pulse of the type which could be provided by a kilohertz repetition rate thin-disk laser [14]. For plasma accelerators driven by long ($\tau_{\mathrm{drive}} \gg T_{\mathrm{pe}}$) drivers, it is important to understand the extent to which the amplitude of the plasma wave decays over the total duration of the driver.

Theoretical studies [15] and measurements of plasma dynamics [16,17] have shown that interactions between the oscillating electrons and the background ions can lead to the growth of instabilities, which dissipate the Langmuir wave energy into higher-order daughter waves. Ultimately, these instabilities lead to the decay of the wakefields and heating of the plasma. In this paper, we present the results of an experimental investigation of the wakefield decay rate in a parameter regime that is relevant for several current and future plasma acceleration schemes, such as plasma wakefield acceleration (PWFA) [6], laser wakefield acceleration (LWFA) [2], and multipulse laser wakefield acceleration (MP-LWFA) [10]. We compare our measured results with particle-in-cell simulations, and show that there is good agreement between theory, simulations, and measurements. We first establish the key

*Present address: NIHR Health Protection Research Unit in Respiratory Infections, Imperial College London, London, United Kingdom.

†Present address: BELLA Center, Lawrence Berkeley National Lab, Berkeley, California, United States.

‡Present address: Deutsches Elektronen-Synchrotron DESY: Hamburg, Germany.

§Present address: Somerville College, Woodstock Road, Oxford OX2 6HD, United Kingdom.

‖simon.hooker@physics.ox.ac.uk

TABLE I. Comparison of key parameters for several experiments to measure the decay of laser-driven plasma waves.

Regime	Target	Plasma	τ_L	n_{e0} (cm^{-3})	$\delta n_e/n_{e0}$	T (eV)	W	τ_L/T_{pe}	$(\lambda_p/\pi\sigma)^2$	$\tau_{\mathrm{wf}}/T_{\mathrm{pe}}$	τ_{wf} (ps)	Ref.
LBWA	Cell	D_2	160 ps	1.07×10^{17}	0.1	20	270	623	0.11	61 ± 59	20.6 ± 20	[18]
SM-LWFA	Jet	He	400 fs	3×10^{19}	0.15	2500	4.6	20	0.023	132 ± 14	1.9 ± 0.2	[19]
SM-LWFA	Jet	He	400 fs	3.7×10^{19}	0.1	1000	5.11	21	0.033	139	1.8	[20]
SM-LWFA	Jet	H_2	400 fs	1×10^{19}	0.1	10	255	11	0.62	142 ± 28	6 ± 1	[21]
SM-LWFA	Jet	He	400 fs	1×10^{19}	0.1	10	255	11	0.62	142 ± 28	6 ± 1	[21]
LWFA	Cell	He	120 fs	1×10^{17}	0.1	14	36	0.34	31.4	33^{+33}_{-8}	8.3^{+8}_{-2}	[22]
LWFA	Jet	He	52 fs	7.4×10^{17}	0.75	13	1150	0.4	1.92	9.7	1.3	[23]
LWFA	Cell	H_2	(48.9 ± 6.3) fs	8.4×10^{17}	0.06	2	705	0.4	0.042	84 ± 25	9 ± 2	This work
LWFA	Cell	D_2	(48.9 ± 6.3) fs	8.4×10^{17}	0.04	2	262	0.4	0.042	134 ± 63	16 ± 8	This work

laser and plasma parameters, which determine the regime in which a laser-plasma accelerator operates. When the quiver velocity of the plasma electrons in the field of the driving laser is nonrelativistic, the wakefield is approximately sinusoidal, and is said to be in the linear regime. For a single, short driving laser pulse, this corresponds to a peak normalized vector potential $a_0 < 1$, where $a_0 = eE/m_e c\omega_0$, E the laser electric field strength, and ω_0 the laser frequency. In this regime, and for the case of a driving laser pulse with Gaussian temporal and transverse intensity profiles, the relative amplitude of the plasma wave $\delta n_e/n_{e0}$ is given by the sum of the relative amplitudes of the radial and longitudinal wakefields [22],

$$\frac{\delta n_e}{n_{e0}} = \frac{\delta n_r}{n_{e0}} + \frac{\delta n_z}{n_{e0}} = A\left[\underbrace{1}_{\text{Long.}} + \underbrace{\left(\frac{2c}{\omega_{\mathrm{pe}}\sigma}\right)^2\left(1-\frac{r^2}{\sigma^2}\right)}_{\text{Radial}}\right] \times \exp\left(\frac{-r^2}{\sigma^2}\right)\sin(\omega_{\mathrm{pe}}\zeta) \tag{1}$$

$$A = \frac{I\sqrt{\pi}}{c^3 n_c m_e}\left(\frac{\omega_{\mathrm{pe}}\tau_L}{2}\right)\exp\left[-\left(\frac{\omega_{\mathrm{pe}}\tau_L}{2}\right)^2\right], \tag{2}$$

where r is the radial distance from the propagation axis of the drive laser, ζ is the temporal delay after the peak of the drive pulse, $\omega_{\mathrm{pe}} = (n_{e0}e^2/m_e\epsilon_0)^{1/2}$ is the plasma frequency, n_{e0} is the plasma electron density, $n_c = \epsilon_0 m_e\omega^2/e^2$ is the critical density, and ω, σ, τ_L, and I are, respectively, the angular frequency, beam radius at the $1/e^2$ intensity, the duration (defined as the half-width at $1/e^2$ intensity) and peak intensity of the driving laser pulse. The ratio of the radial to the longitudinal wakefield components at $r = 0$ is $\delta n_r/\delta n_z|_{r=0} = (2c/\omega_{\mathrm{pe}}\sigma)^2 = (\lambda_p/\pi\sigma)^2$, where $\delta n_r/\delta n_z \gg 1$ indicates a predominantly radial wakefield and $\delta n_r/\delta n_z \ll 1$ indicates a longitudinal wakefield, which we will refer to as a one-dimensional (1D) wakefield.

The mechanisms responsible for the decay of laser-driven plasma waves have been investigated in several earlier studies. Marquès *et al.* [22] found that radial-dominated and longitudinal-dominated wakefields can have different decay mechanisms. Longitudinal wakefields decay through collisions [24], Landau damping [25], beam loading by accelerated particles [19], and the modulational instability [15]. The growth rate of the modulational instability is expected to be much greater than the collisional or Landau damping mechanisms, and hence will usually dominate the decay in the case when beam loading is not significant. If the total charge trapped and accelerated by the wakefield is large, then beam loading becomes important, and can be the leading cause of the wakefield decay [19]. Radial wakefields can decay via an additional mechanism. When the radial plasma density is nonuniform, electrons at different radial trajectories have different oscillation periods, which leads to a loss of coherence of the plasma oscillation. This can happen, e.g., via a final radial extent of the drive laser or beam, or in preformed plasma channels [26–29].

In addition to the ratio $\delta n_r/\delta n_z$, two other parameters are important in determining the mechanisms responsible for, and the rate of, wakefield decay. First, the ratio of the energy density of the Langmuir wave to the thermal energy density, $W = (v_L/v_t)^2 = \epsilon_0|\mathbf{E_L}|^2/2n_{e0}k_B T_e$, where $v_L = eE_L/m_e\omega_{\mathrm{pe}}$, $v_t = (k_B T_e/m_e)^{1/2}$, E_L is the electric field strength of the wakefield, k_B is the Boltzmann constant, and T_e is the electron plasma temperature [15]. The parameter W determines the growth rate of the modulational instability and delineates the strong-field regime ($W \gg 1$) from the weak-field regime ($W \lesssim 1$). Second, the ratio of the drive pulse length to the plasma ion period τ_L/T_{pi}, where $T_{\mathrm{pi}} = 2\pi/\omega_{\mathrm{pi}}$, where $\omega_{\mathrm{pi}} = (Zn_{e0}e^2/M\epsilon_0)^{1/2}$, and in which Z and M are the charge and mass of the ions respectively. For $\tau_L \gg T_{\mathrm{pi}}$ the plasma instabilities driven by ion dynamics coevolve with the drive laser, and for $\tau_L \ll T_{\mathrm{pi}}$ they develop only after the wakefield is excited.

Table I summarizes the results of previous measurements of the decay time of laser-driven wakefields. The penultimate and antepenultimate columns of the table give the wakefield decay time τ_{wf} and the ratio of this to the electron plasma period T_{pe}. It should be noted that the precise definition of τ_{wf} varies between the experiments. In Refs. [18,21] it refers to the total length of the detectable wakefield signal, whereas in Refs. [19,20,22,23], and in the present work, it refers to the time taken for the wakefield amplitude to decay to $1/e$ of the maximum amplitude. We also note that the time given in Ref. [18] refers to the saturation time of the beat-wave-driven wakefield, and, for simplicity, we have taken this to be equal to the decay time. It is striking that with the exception of Ref. [23], the ratio of the wakefield lifetime to the electron plasma period $\tau_{\mathrm{wf}}/T_{\mathrm{pe}}$ varies by less than a factor of 5 in experiments for which the plasma density and the duration of the drive pulse both vary by more than two orders of magnitude.

The earlier work summarized in Table I was undertaken in a wide range of laser-plasma accelerator regimes. In the experiment by Moulin *et al.* [18] a wakefield was excited using the beat-wave (LBWA) scheme in which two long pulses (160 ps and 90 ps), of angular frequencies ω_1 and ω_2, interfere to generate a beat pattern at the plasma frequency $\omega_{pe} = \omega_1 - \omega_2$. In that work plasma instabilities therefore developed during the excitation of the wakefield by the drive beam or drivers. The experiments by Leblanc *et al.* [19], Chen *et al.* [20], and Ting *et al.* [21] corresponded to the self-modulated laser wakefield (SM-LWFA) regime in which interaction between a long laser pulse ($\tau_L \gg T_{pe}$) and the weak plasma wave it drives causes the laser pulse to become modulated with a period of T_{pe}, leading to a nonlinear feedback in which the modulation of the laser pulse and the wakefield amplitude both increase with delay relative to the front of the driving pulse. Hence these experiments correspond to an intermediate regime in which the duration of the drive pulse lies between the electron plasma period and the ion plasma period T_{pi}. Finally, Marquès *et al.* [22] and Kotaki *et al.* [23] performed experiments in the LWFA regime originally proposed by Tajima and Dawson, in which the wakefield is excited by a laser pulse with $\tau_L < T_{pe}$. These last two experiments both operated in the radial-dominated wakefield regime, and shorter decay times relative to the plasma period were observed compared to the experiments that generated longitudinal-dominated wakefields. With the exception of the work by Kotaki *et al.* [23], in all the experiments $\delta n_e/n_{e0} \approx 0.1$, i.e., they were all conducted in the linear wakefield regime. We note that for the much stronger wakefields ($\delta n_e/n_{e0} \approx 0.75$) studied in Ref. [23], the observed ratio τ_{wf}/T_{pe} is much smaller than found in experiments operating in the linear regime; this finding is discussed further in Sec. IV.

Before concluding this short review of prior experimental work, we note that wakefield decay and ion motion has also been studied for proton-beam-driven wakefield accelerators [30]; these results have not been included in Table I owing to the very different driver and plasma parameters. We also note recent experiments to establish the limits to the repetition rate of PWFAs driven by electron bunches [31]. The topic of the present paper, the timescale for wakefield decay, is related to the maximum possible repetition rate of a plasma accelerator. However, we emphasize that wakefield decay is just the first step in a complex chain of processes, which includes wakefield decay, electron-ion recombination, and heat redistribution, which must be completed before the following drive pulse can be delivered.

The work presented in the present paper is a measurement of the decay rate of a one-dimensional ($\delta n_r/\delta n_z \ll 1$), linear wakefield ($a_0 \sim 0.5$) in the short-pulse LWFA regime ($\tau_L/T_{pe} \approx 0.4$). This short-pulse regime is relevant for future plasma wakefield facilities [32–34] (although we note that some of these are expected to operate in the quasilinear regime ($a_0 \sim 1$ for a single pulse), e.g., Ref. [32]), and it is also relevant to alternative schemes, such as MP-LWFAs [10,11,13].

II. MEASUREMENT OF THE WAKEFIELD LIFETIME

Experiments to measure the lifetime of a plasma wakefield in the 1D linear regime were undertaken at the Central Laser Facility of the Rutherford Appleton Laboratory, using the Astra-Gemini TA3 laser. A schematic illustration of the experiment layout is shown in Fig. 1.

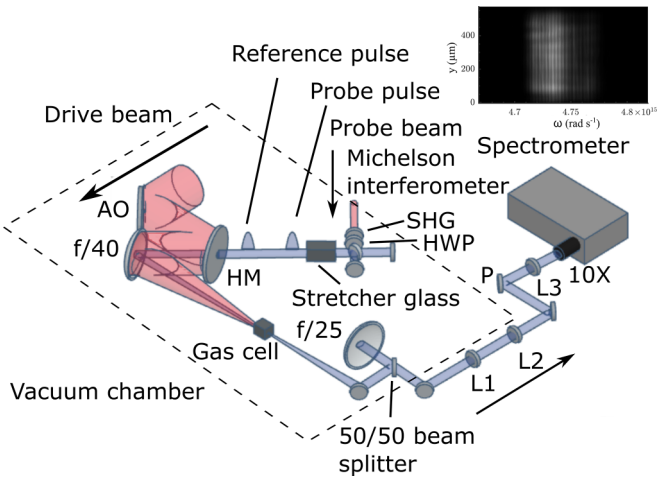

FIG. 1. Schematic drawing of the experimental layout inside the target vacuum chamber. Both beams of the Astra-Gemini TA3 laser were used: one as the drive beam, and the other as the diagnostic probe beam. The 800 nm beams are shown in red and the 400 nm diagnostic beam is shown in blue. After leaving the gas cell, the diagnostic beam was transported to a 400 nm spectrometer located outside the vacuum chamber. The inset shows an example recording of a wakefield in a spectral interferogram, as captured by the spectrometer camera. AO: Adaptive optic; HM: Holed mirror; HWP: Half-wave plate; L1: f = 500 mm lens; L2: f = −100 mm lens; L3: f = 300 mm lens; P: polariser; 10X: microscope objective; SHG: second harmonic generating crystal.

A linearly polarized laser pulse with energy $E = (1.68 \pm 0.06)$ J, center wavelength 800 nm, and FWHM pulse duration (48.9 ± 6.3) fs was used to drive the wakefield. This pulse was focused by an on-axis reflecting paraboloid of focal length $f \approx 6.1$ m, used at $f/40$, to a spot size ($1/e^2$ intensity radius) of $w_0 = (52.3 \pm 0.8)$ μm at the center of a gas cell. The peak intensity at the laser focus was $I = 6.5\times10^{17}$ W cm^{-2}. The peak fluence of the focal spot, measured using the transverse fluence profile, was used to calculate the peak normalized vector potential $a_0 = 0.54 \pm 0.18$, with approximately a factor of 0.3 of the beam energy enclosed within the FWHM beam diameter at focus.

Laser radiation could enter and leave the cell via a pair of coaxial, 400 μm diameter pinholes located at each end of the 4 mm long gas cell. Gas, either hydrogen (H_2) or deuterium (D_2), was flowed into the cell in a pulse of duration of approximately 500 ms; the gas flowed into the surrounding vacuum chamber via the pinholes. For these experiments the cell backing pressure was $P_{cell} = (17.0 \pm 1.2)$ mbar, corresponding to an electron density 8.4×10^{17} cm^{-3} (assuming 100% ionization).

The amplitude of the plasma wave was measured by frequency domain holography (FDH) [35], analyzed with the TESS technique [36,37]. In this method, two chirped and stretched diagnostic pulses are generated: (i) a probe pulse, which propagates behind the drive pulse, and acquires a temporally dependent phase shift from the density modulation of the plasma wave; and (ii) a near-identical reference pulse,

which propagates ahead of the drive pulse. This pair of diagnostic pulses was generated by passing a frequency-doubled pick off from the probe beam through a Michelson interferometer with a path difference corresponding to $\Delta\zeta \approx 6$ ps. Each of the pair of pulses thereby created was then frequency chirped and stretched to a duration of 1.35 ps by propagating them through a 160 mm long piece of glass (BK7). The diagnostic pulses were injected coaxially with the drive beam by directing them through a holed turning mirror, and focused into the gas cell by the same optic used to focus the drive beam. On leaving the gas cell the diagnostic pulses were separated from the transmitted drive pulse by reflection from a dichroic mirror and imaged onto the entrance slit of a Czerny-Turner spectrometer to yield a spectral interferogram, which was recorded by a CCD camera (Andor Newton DU940N-BU). The wakefield amplitude was calculated from the captured interferograms using the TESS technique, as follows. Each spectral interferogram was Fourier transformed along its spectral axis to give a spatiotemporal profile. The Fourier-transformed data comprises a zero-frequency (DC) band; a sideband located at $t = \Delta\zeta$; and three satellites—two on either side of the sideband, and a third located near the DC band. These satellites arise from the phase shift imposed on the probe beam by the sinusoidal plasma wave. The satellites are offset from the sideband and have temporal locations given by Refs. [36,37],

$$\tau = \Delta\zeta \pm \varphi^{(2)}\omega_{\mathrm{pe}}, \tag{3}$$

where $\varphi^{(2)}$ is the group delay dispersion (GDD) of the probe and reference pulses. Equation (3) was used, together with the group delay dispersion and cell backing pressure, to define the expected location of the satellites. These were found to be fully separated from the sideband, and close to their expected locations. For plasma waves with large amplitudes, higher-order satellites can appear, located at $\tau = \Delta\zeta \pm m\varphi^{(2)}\omega_{\mathrm{pe}}$, $m = 2, 3, 4, \ldots$, but these higher-order satellites were not observed in this experiment. The relative amplitude of the wakefield at delay ζ can be found from the ratio r of the satellite amplitude to that of the sideband since this is given by Refs. [36,37],

$$r = \mathcal{F}(\omega_{\mathrm{pe}})\frac{J_1(\phi_0)}{J_0(\phi_0)}, \tag{4}$$

where,

$$\phi_0 = \frac{\omega_{\mathrm{pe}}^2 L}{2\omega_{\mathrm{probe}} c}\frac{\delta n_e}{n_{e0}}. \tag{5}$$

and where J_0 and J_1 are Bessel functions of the first kind, $\mathcal{F}(\omega_{\mathrm{pe}})$ a spectral overlap function (see Appendix), L is the interaction length, and ω_{probe} is the frequency of the probe laser. By varying the backing pressure, and measuring ω_{pe} immediately after the drive pulse, we could confirm that the measured positions of the identified satellites closely followed the expected positions, based on Eq. (3). Using this procedure, it was found that the pressure in the cell was linearly related to the measured backing pressure through $P_{\mathrm{cell}} = \alpha(P_{\mathrm{gauge}} - P_0)$, where $\alpha = 0.96$ accounts for the fact that the pressure guage was located prior to the gas cell gas inlet and $P_0 = 3$ mbar (see Appendix).

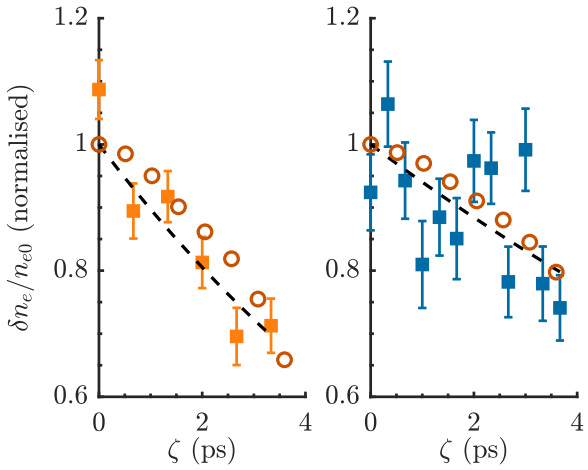

FIG. 2. Measured normalized relative wakefield amplitude calculated using the TESS technique [36,37] as a function of delay for: (a) hydrogen; (b) deuterium, recorded with a backing pressure $P_{\mathrm{cell}} = (17.0 \pm 1.2)$ mbar. For each delay are shown the uncertainty-weighted average wakefield amplitude ($\delta n_e(\zeta)/n_{e0}$) and the standard error. The uncertainty was calculated using the background noise in the Fourier-transformed interferograms. The wakefield amplitude calculated from the PIC simulations are shown as open circles. Also shown are fits of the exponential function to the data as black lines.

III. RESULTS

The wakefield amplitude was measured for a range of delays ζ in steps of 0.67 ps. For each temporal delay, the results of ten shots were averaged in order to reduce the statistical error in the measured wake amplitude.

Figure 2 shows, for hydrogen and deuterium, the measured wakefield amplitude as a function of delay, normalized to $\delta n_e(0)$, where $\delta n_e(0)$ is determined by a fit of the function $\delta n_e(\zeta) = \delta n_e(0)\exp(-\zeta/\tau_{\mathrm{wf}})$ to the data. Due to variations in the experimental conditions, the plasma waves driven in deuterium had an initially lower amplitude, which made the error bars relatively larger after normalization.

Also shown in Fig. 2 are the results of 2D particle-in-cell (PIC) simulations performed with the relativistic particle-in-cell code SMILEI (Simulation of Matter Irradiated by Light at Extreme Intensities [38]) for the laser and plasma parameters used in the experiment (see Appendix). The wakefield amplitude was calculated from the maximum Fourier amplitude (near ω_{pe}) of the density variation $\delta n(x, y) = \delta n_e(x, y) - \delta n_i(x, y)$ corresponding to the wakefield plasma oscillation, where $\delta n_i(x, y)$ is the ion density. The Fourier amplitude, A_F, was converted to the wakefield amplitude, A_{wake} using the relation $A_{\mathrm{wake}} = 2A_F\Delta x/[\int W_T^\beta(x)\,dx]$. Here $W_T^\beta(x)$ is a Tukey window with window parameter β (set to $\beta = 0.2$), and $\Delta x = 26.7$ nm, the simulation cell size in the dimension along the laser axis of propagation.

The results of the simulations are seen to be in very good agreement with the experimental data. As well as correctly reproducing the timescale of the wakefield decay, the wakefield amplitudes calculated by the simulations are found to be close in absolute terms to the measured values. For both hydrogen and deuterium plasmas the relative wake amplitude at $\zeta = 0$ was calculated to be 7.5% for the laser and plasma conditions

TABLE II. Comparison of the wakefield decay times (in picoseconds) obtained from experiments and PIC simulations.

	$\tau_{wf}^{H_2}$	$\tau_{wf}^{D_2}$	$\tau_{wf}^{D_2}/\tau_{wf}^{H_2}$
Experiment	9 ± 2	16 ± 8	1.78 ± 0.97
Simulation	8.5 ± 0.9	15 ± 1	1.76 ± 0.22

of the experiment. This compares with the measured values of $(6 \pm 2)\%$ for hydrogen and $(4 \pm 2)\%$ for deuterium. This agreement, which is within a factor of two, is remarkably good when it is considered that: (i) the simulations contained no free parameters; and (ii) the measured wakefield amplitude is rather sensitive to variations in many of the experimental parameters. These experimental parameters include: the pulse energy, duration, and spatiotemporal quality of the laser pulse; the spectrum of the probe pulse; the relative alignment of the drive and diagnostic pulses; and the pressure in the gas cell. Notably, a large contributor to less than optimal conditions was the relatively poor quality of the laser focal spot, with only a factor 0.3 of the beam energy enclosed within the FWHM beam diameter at focus. In the simulations, an ideal focal spot was used, albeit with the same peak a_0 as estimated from the experimental parameters.

Table II summarizes the results of the measurements and simulations; to enable a comparison with the experiments, the temporal variation of the wake amplitude found in the simulations was fitted to an exponential decay. While the decay process is not expected to be strictly exponential [39], as is evident from the results of PIC simulations shown in Fig. 2. However, we chose to fit the data to an exponential decay since it is a reasonable approximation and it provides a convenient measure for comparing (in Table I) the results of experiments undertaken over a wide range of plasmas parameters. For the conditions of the experiment we find: for hydrogen, $\tau_{wf} \approx 9$ ps, corresponding to around 76 plasma periods; for deuterium these values are approximately 16 ps and 134 periods, respectively.

The measured wakefield lifetimes are long compared to the electron plasma period $T_{pe} = 121$ fs, and are comparable to the ion plasma periods $T_{pi} = 5.2$ ps and 7.4 ps for hydrogen and deuterium, respectively. The ratios of the decay times measured for deuterium and hydrogen are found to be $\tau_{wf}^{D2}/\tau_{wf}^{H_2} = 1.78 \pm 0.97$ and 1.76 ± 0.22 from the measurements and simulations, respectively. The experimentally measured decay times are seen to be in very close agreement with those determined from PIC simulations. Unfortunately the experimental errors, particularly those for D_2, which had a lower initial wake amplitude due to less optimized experimental conditions—the experiment was optimized once per day and the D_2 data was collected after the H_2 data the same day—and therefore a lower signal-to-noise ratio, are too large to conclude that the ratio $\tau_{wf}^{D2}/\tau_{wf}^{H2}$ differs from unity. However, the PIC simulations do show that the decay time for deuterium is longer than that for hydrogen, and that their ratio is close to, but larger than, the ratio of the ratio of the inverse ion plasma frequencies $\omega_{D2}^{-1}/\omega_{H2}^{-1} = \sqrt{M_{D2}/M_{H2}} = \sqrt{2}$. The measurements and simulations demonstrate that the wake decay time is of the order of the inverse ion plasma period, but that it is too simplistic to assume that the decay time is strictly proportional to this quantity [39].

A detailed analysis of the PIC simulations [39], and comparison with work by Sanmartin *et al.* [40], shows plasma waves under these experimental conditions decay via the modulational instability. This instability causes small spatial variations in the ion density to grow exponentially, with a timescale of order T_{pi}, leading to a loss of coherence of the electron oscillations, and hence decay of the wakefield amplitude.

IV. CONCLUSION

In conclusion, we have used single-shot frequency domain holography to measure the lifetime of 1D linear plasma wakefields in hydrogen and deuterium plasmas driven in the short-pulse LWFA regime. Wakefields with relative amplitudes of approximately 6% were driven by 1.7 J, 50 fs laser pulses in hydrogen and deuterium plasmas of density $n_{e0} = 8.4 \times 10^{17}$ cm^{-3}. The wakefield lifetimes were measured to be $\tau_{wf}^{H_2} = (9 \pm 2)$ ps and $\tau_{wf}^{D_2} = (16 \pm 8)$ ps, respectively, for hydrogen and deuterium. The experimental results were found to be in very good agreement with 2D particle-in-cell simulations.

These findings are of relevance to the MP-LWFA scheme, in which the wakefield is driven resonantly by a train of short pulses [10,11]. This latter approach is of considerable interest since it offers a route to driving LWFAs at high pulse repetition rates with novel laser technologies, which can provide the required average power, with high wall-plug efficiency, but which deliver pulses, which are too long to drive a plasma wave directly. The wakefield lifetime is of key importance to the MP-LWFA scheme since it determines the maximum useful number of pulses in the pulse train. For example, in the plasma-modulated plasma accelerator (P-MoPA) scheme [13], plasma modulation of $a \sim$ 1 ps, 1.7 J pulse is used to generate a train of ~ 5 pulses. Simulations show that this train can resonantly excite a wakefield of amplitude $\delta n_e/n_{e0} = 0.6$ in a plasma of density $n_{e0} = 2.5 \times 10^{17}$ cm^{-3}. The results presented in the present paper will be relevant to this scheme, at least during the crucial period in which the wakefield grows to a large amplitude. The experiments described in Ref. [23], summarized in Table I, indicate that the decay rate of large amplitude wakes is faster than for linear wakefields. However, the authors of that earlier work note that the measured decay rate may have been increased by nonuniformities in the gas jet target that was used. It is clear, therefore, that further work is required to determine the wakefield decay rate in the nonlinear regime.

The work presented here shows that, for plasma densities relevant to MP-LWFAs, the wakefield lifetime corresponds to of order 100 plasma periods, which is large compared to the $N \approx 10$ pulses required for MP-LWFA schemes driven by pulse trains of total duration in the picosecond range [13].

ACKNOWLEDGMENTS

This work was supported by the UK Science and Technology Facilities Council (STFC UK) (Grants No. ST/N504233/1, No. ST/P002048/1, No. ST/R505006/1,

No. ST/S505833/1, and No. ST/V001655/1]; the Engineering and Physical Sciences Research Council (EPSRC) (EP/N509711/1, EP/V006797/1), and the Central Laser Facility; the Plasma HEC Consortium (Grant No. EP/R029149/1), and the ARCHER UK national supercomputing service. This material is based upon work supported by the Air Force Office of Scientific Research under Award No. FA9550-18-1-7005. This work was supported by the European Union's Horizon 2020 research and innovation programme under Grant Agreements No. 653782 and No. 730871. This research was funded in whole, or in part, by EPSRC and STFC, which are Plan S funders. For the purpose of Open Access, the author has applied a CC BY public copyright licence to any Author Accepted Manuscript version arising from this submission.

The data associated with this paper, and the input decks used for the PIC simulations are available online [41].

APPENDIX

In this Appendix we provide further details of the experimental setup, the TESS method and associated calibrations, and the particle-in-cell simulations.

1. Experimental setup

The diagnostic pulses were generated using one of the Gemini beams (central wavelength 800 nm), temporally synchronized with the drive beam. This beam was frequency doubled to 400 nm and split into two temporally offset pulses using a Michelson interferometer with a path difference corresponding to $\Delta\zeta \approx 6$ ps between the two arms. The pulses were subsequently chirped, and stretched to a pulse duration of approximately 1.35 ps, by propagating them through a 160 mm long piece of BK7 glass. The diagnostic pulses were injected co-axially with the drive beam by directing them through a holed mirror, and on leaving the gas cell they were reflected by a dichroic mirror and a beam splitter and directed at normal incidence to a spherical mirror of focal length $f = 2.5$ m ($f/25$). The collimated light from the object plane, located a distance f from the spherical mirror, was returned through an optical wedge onto a set of lenses: L1: $f = 500$ mm and L2: $f = -100$ mm forming a down-collimating telescope; L3: $f = 300$ mm; and a $10X$ microscopic lens ($f = 20$ mm) used to image the beam onto the spectrometer.

A half-wave plate (HWP) and polarizer setup was used to filter out blue light generated in the plasma by the drive beam. A simplified drawing of the layout is shown in Fig. 3.

The peak intensity of the drive pulse at focus was estimated by using a camera to record the transverse fluence profile of the focus. This was converted to a transverse intensity profile by using the measured energy and duration of the pulse.

2. Spectral phase

The spectral phases of the diagnostic pulses (i.e., the probe and reference pulses) were measured by recording the spectrum of the relevant diagnostic pulse after it had copropagated through the gas cell with the driver pulse. A sharp reduction

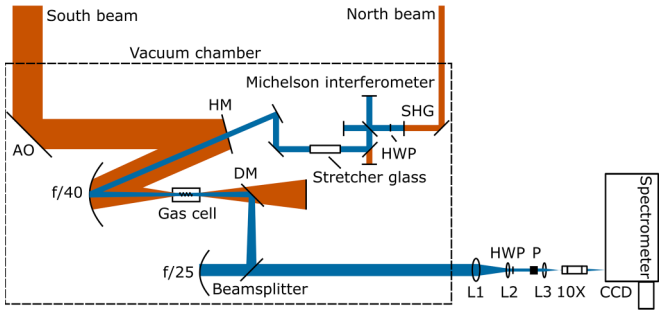

FIG. 3. Schematic drawing of the experimental layout inside the target vacuum chamber. Both beams of the Astra-Gemini TA3 laser were used, one beam used as the drive beam and the other beam as the diagnostic beam. The 800 nm beams are shown in red and the 400 nm diagnostic beam is shown in blue. The diagnostic beam was transported to a 400 nm imaging spectrometer located outside the vacuum chamber. AO: adaptive optic; SHG: second harmonic generating crystal; HWP: half wave plate; P: polarizer; L1: $f = 500$ mm (4 in diameter); L2: $f = -100$ mm (1 in diameter); L3: $f = 300$ mm (1 in diameter).

in the spectral intensity of the diagnostic pulse was observed at the local frequency corresponding to the point in the probe pulse, which overlapped with the drive pulse. This reduction of intensity was caused by the high refractive gradient at the ionization front produced by the drive pulse. By tracking, as a function of the relative delay ζ_i of the drive pulse, the frequency at which this intensity reduction occurred, it was possible to measured the local frequency $\omega(\zeta_i)$ of the diagnostic pulse. An example measurement is shown in Fig. 4, for one temporal delay.

The measured frequency $\omega(\zeta_i)$ was used to estimate the spectral phase in the following way. By measuring the probe spectrum separately on a spectrometer we obtained its spectral amplitude $|\mathcal{E}(\omega)|$, from which we could reconstruct the spectral representation of its electric field as $\mathcal{E}(\omega) = |\mathcal{E}(\omega)| \exp[\varphi(\omega)]$. Here $\varphi(\omega)$ is the spectral phase to be estimated, assumed to be a third-order polynomial:

$$\varphi(\omega) = \varphi_0 + \varphi_1(\omega - \omega_0) + \tfrac{1}{2}\varphi_2(\omega - \omega_0)^2 + \tfrac{1}{6}\varphi_3(\omega - \omega_0)^3,$$

where the coefficients φ_1, φ_2, and φ_3 are to be determined. By guessing initial values for these coefficients, the temporal representation of the electric field can be obtained from the

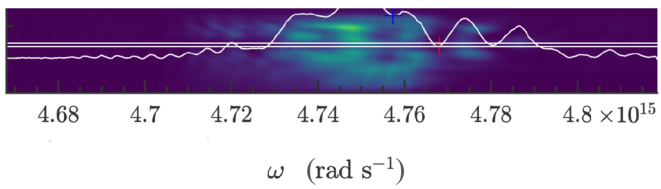

FIG. 4. Plot of the perturbed spectrum of the probe pulse, taken during measurements of the spectral chirp of the probe pulse. The temporal overlap of the probe and drive pulses in the gas cell causes a reduction of the probe pulse intensity as measured on the spectrometer. The red cross marks a low-intensity feature that is tracked as a function of the temporal delay between the drive and probe (or reference) pulses, in order to measure the spectral phase.

Fourier transform of $\mathcal{E}(\omega)$, $E(\zeta) = \mathrm{FT}[\mathcal{E}(\omega)]$. The temporal phase is obtained from its argument: $\phi(\zeta) = \arg[E(\zeta)]$. Noting that the instantaneous frequency is given by the derivative of the temporal phase, $\omega(\zeta) = d\phi(\zeta)/d\zeta$, we compared this reconstructed frequency with the measured frequency $\omega(\zeta_i)$ using the overlap technique described above. We could improve on the guess of the spectral phase $\varphi(\omega)$ and find the value that best matched the measured instantaneous frequency by minimizing the squared difference between these:

$$\min \sum_i \left(\left| \omega_{\mathrm{probe,ref}}(\zeta_i) - \frac{d\phi(\zeta_i)}{d\zeta} \right|^2 \right). \tag{A1}$$

Using this technique, φ_2 (i.e., the GDD) was found to be $(18600 \pm 790)\,\mathrm{fs}^2$ and $(17600 \pm 800)\,\mathrm{fs}^2$ for the probe [Fig. 5(a)] and references pulses [Fig. 5(b)], respectively. These values were used in the TESS analysis.

3. TESS analysis method

TESS is a simplified analysis method to obtain the wakefield amplitude from spectral interferometric data obtained using an FDH diagnostic setup. Following Matlis *et al.* [36], let a propagating reference pulse, ahead in time of the pump and probe pulses, and a probe pulse copropagating with the wakefield be described by $E_{\mathrm{ref}}(\zeta)$ and the phase-modulated probe pulse by $E'_{\mathrm{probe}}(\zeta) = E_{\mathrm{probe}}(\zeta)\exp[i\phi_0 \sin(\omega_{\mathrm{pe}}\zeta)]$, where the wakefield is assumed to be sinusoidal with ϕ_0 being the phase amplitude of the sinusoidal wave, and ω_{pe} the plasma frequency. Taking the Fourier transform of the probe pulse one obtains

$$\begin{aligned}
\mathcal{E}'_{\mathrm{probe}}(\omega) &= \frac{1}{\sqrt{2\pi}} \int_{-\infty}^{\infty} E_{\mathrm{probe}}(\zeta) \\
&\quad \times \exp[i\phi_0 \sin(\omega_{\mathrm{pe}}\zeta)] \exp(-i\omega\zeta) d\zeta . \qquad \text{(A2)} \\
&= \frac{1}{\sqrt{2\pi}} \int_{-\infty}^{\infty} E_{\mathrm{probe}}(\zeta) \sum_{-\infty}^{\infty} J_k(\phi_0) \\
&\quad \times \exp(ik\omega_{\mathrm{pe}}\zeta) \exp(-i\omega\zeta) d\zeta \qquad \text{(A3)} \\
&= \sum_{k=-\infty}^{\infty} J_k(\phi_0) \mathcal{E}_{\mathrm{probe}}(\omega - k\omega_{\mathrm{pe}}), \qquad \text{(A4)}
\end{aligned}$$

using the Jacobi-Anger expansion to express the phase term as an infinite sum of Bessel functions of the first kind:

$$\exp[i\phi_0 \sin(\omega_{\mathrm{pe}}\zeta)] = \sum_{k=-\infty}^{\infty} J_k(\phi_0) \exp(ik\omega_{\mathrm{pe}}\zeta). \tag{A5}$$

The spectral interference intensity between the probe and reference pulses is given by:

$$S(\omega) = |\mathcal{E}_{\mathrm{probe}}(\omega) + \mathcal{E}_{\mathrm{ref}}(\omega)|^2. \tag{A6}$$

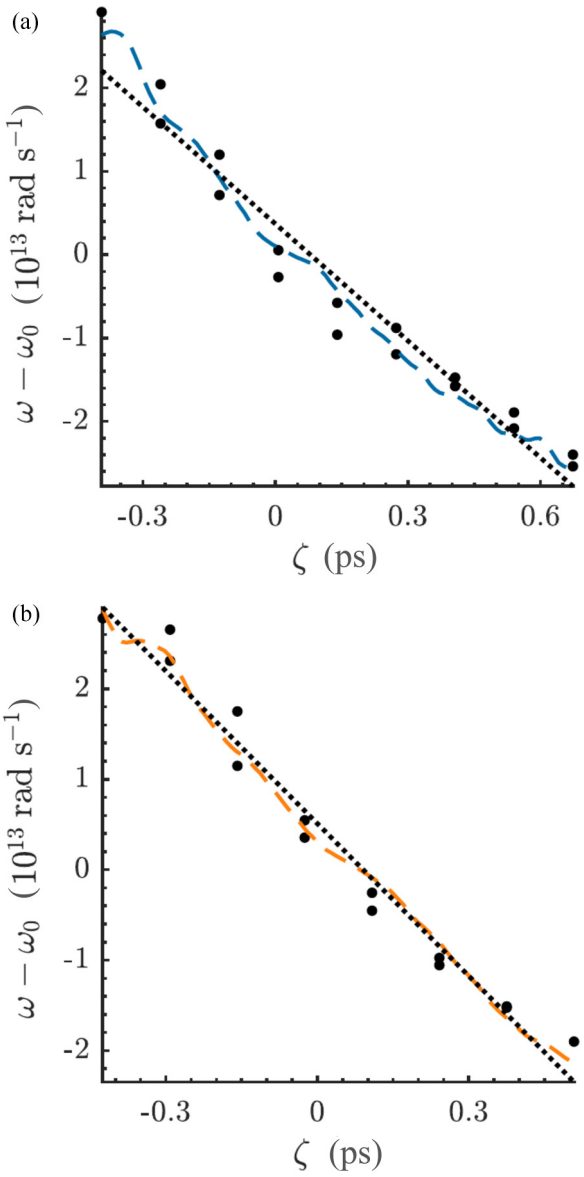

FIG. 5. Measurement of the spectral phase of the (a) probe and (b) reference pulses. The black dots indicate the location of the ionization front feature in time and frequency. The dashed lines show the fitted first derivative of the temporal phase $d\phi(\zeta)/d\zeta$ of each pulse. The dotted lines show a linear fit to the data.

Using Eq. (A4), this can be expanded into a sum of the cross terms of the probe and reference spectra, as well as the different copies contained in the probe spectrum:

$$\begin{aligned}
S(\omega) &= |\mathcal{E}_{\mathrm{probe}}(\omega)|^2 + |\mathcal{E}_{\mathrm{ref}}(\omega)|^2 + \mathcal{E}^*_{\mathrm{probe}}(\omega)\mathcal{E}_{\mathrm{ref}}(\omega) + \mathrm{c.c.} \qquad \text{(A7)} \\
&= \sum_{m,n} J_n(\phi_0) J_m(\phi_0) \mathcal{E}^*_{\mathrm{probe}}(\omega - n\omega_{\mathrm{pe}}) \mathcal{E}_{\mathrm{probe}}(\omega - m\omega_{\mathrm{pe}}) + |\mathcal{E}_{\mathrm{ref}}(\omega)|^2 \\
&\quad + \sum_k J_k(\phi_0) \mathcal{E}^*_{\mathrm{ref}}(\omega) \mathcal{E}_{\mathrm{probe}}(\omega - k\omega_{\mathrm{pe}}) \exp(-i\omega\Delta\zeta) + \mathrm{c.c.}, \qquad \text{(A8)}
\end{aligned}$$

where c.c. stands for the complex conjugate of the previous term, and the Fourier shift theorem was used to introduce $\Delta\zeta$, the temporal delay between the probe and reference pulses. The Fourier transform of the spectral interferogram in Eq. (A8) is given by:

$$S(\zeta) = \sum_m g_m(\phi_0, \zeta, \omega_{\rm pe}) H(\zeta, m\omega_{\rm pe}) + H(\zeta, 0) \quad \text{(A9)}$$

$$+ \sum_k J_k(\phi_0) H(\zeta - \Delta\zeta, k\omega_{\rm pe}) + \text{c.c.}, \quad \text{(A10)}$$

where the function H is given by:

$$H(\zeta, \omega_{\rm pe}) = \frac{1}{\sqrt{2\pi}} \int_{-\infty}^{\infty} \mathcal{E}^*_{\rm ref}(\omega) \mathcal{E}_{\rm probe}(\omega - \omega_{\rm pe}) \exp(i\omega\zeta) d\omega, \quad \text{(A11)}$$

and the function g by:

$$g_m(\phi_0, \zeta, \omega_{\rm pe}) = \sum_n J_n(\phi_0) J_{m+n}(\phi_0) \exp(in\omega_{\rm pe}\zeta). \quad \text{(A12)}$$

This can be rewritten as, defining $H_0(\zeta) \equiv H(\zeta, \omega_{\rm pe} = 0)$

$$S(\zeta) = \underbrace{\sum_m g_m(\phi_0, \zeta, \omega_{\rm pe}) f(m\omega_{\rm pe}) H_0(\zeta + m\tau) + H_0(\zeta)}_{\text{DC peak}} \quad \text{(A13)}$$

$$+ \underbrace{\sum_k J_k(\phi_0) \mathcal{F}(k\omega_{\rm pe}) H_0(t - \Delta\zeta + k\tau) + \text{c.c.},}_{\text{Sidebands+satellites}} \quad \text{(A14)}$$

where $\tau \equiv \varphi^{(2)}\omega_{\rm pe}$, and $\mathcal{F}(k\omega_{\rm pe})$ is a spectral overlap factor, which in general is given by [37]:

$$\mathcal{F}(k\omega_{\rm pe}) = \frac{\int_{-\infty}^{\infty} |\mathcal{E}_{\rm probe}(\omega + k\omega_p)||\mathcal{E}_{\rm ref}(\omega)| d\omega}{\int_{-\infty}^{\infty} |\mathcal{E}_{\rm probe}(\omega)||\mathcal{E}_{\rm ref}(\omega)| d\omega}. \quad \text{(A15)}$$

The measured probe and reference spectra and their spectral overlap factors are plotted in Fig. 6.

The sideband term in Eq. (A14) contains TESS satellite intensity peaks ($k \neq 0$) and the sideband caused by interference ($k = 0$). These peaks are plotted in Fig. 7. In this figure is also shown the dependence on the temporal separation between the TESS satellite peaks and the sideband term with plasma density, due to variation of the $\omega_{\rm pe}$ term in τ. The ratio r between the first TESS satellite in Eq. (A14) ($k = 1$ term, evaluated at $\zeta = \Delta\zeta - \tau$) and the sideband ($k = 0$ term, evaluated at $\zeta = \Delta\zeta$), is

$$r = \frac{J_1(\phi_0)\mathcal{F}(\omega_{\rm pe})}{J_0(\phi_0)}. \quad \text{(A16)}$$

For small amplitudes $\phi_0 \ll 1$, the Bessel functions of the first kind J_α can be expanded as:

$$J_\alpha(\phi_0) \approx \frac{1}{(\alpha - 1)!} \left(\frac{\phi_0}{2}\right)^\alpha, \quad \text{(A17)}$$

with $J_0(\phi_0) \approx 1$ and $J_1(\phi_0) \approx \phi_0/2$. The phase amplitude ϕ_0 can therefore be expressed as:

$$\phi_0 = \frac{2r}{\mathcal{F}(\omega_{\rm pe})}. \quad \text{(A18)}$$

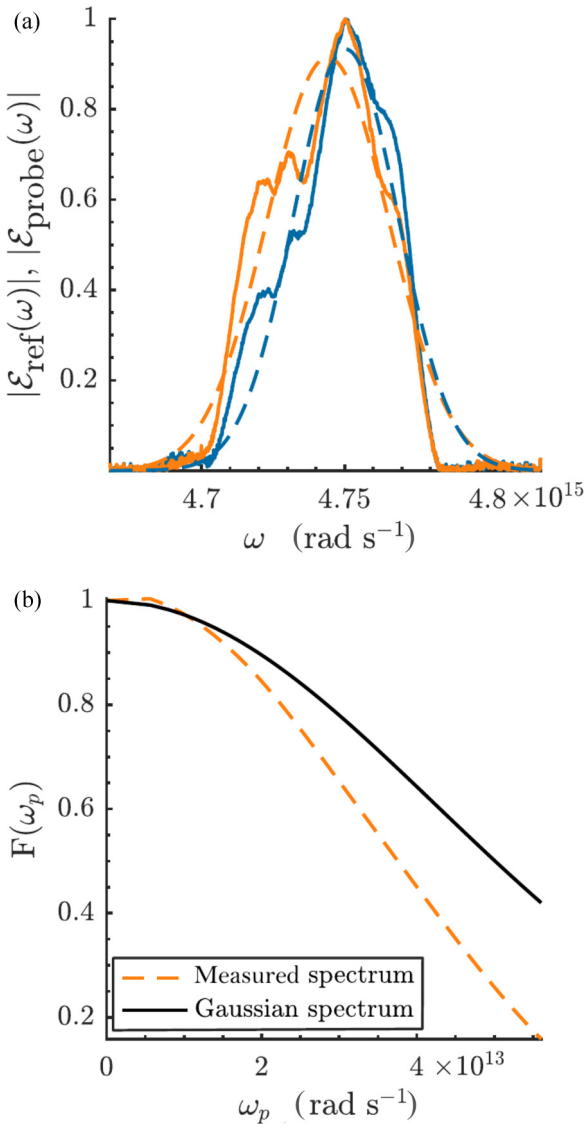

FIG. 6. (a) Line outs of the spectral intensities of the probe (red line) and reference pulses (blue line). The dashed lines show Gaussian fits to these spectra. (b) spectral overlap function $\mathcal{F}(\omega_{\rm pe})$ as a function of the plasma frequency, for the measured spectra and Gaussian spectra fitted to the measured spectra.

The plasma wave is assumed to be sinusoidal:

$$n_e(\zeta) = n_{e0} + \delta n_e \sin(\omega_{\rm pe}\zeta). \quad \text{(A19)}$$

The phase difference acquired by a laser of wavelength λ propagating through plasma is given by:

$$\Delta\phi(\zeta) = \int \frac{n_e(\zeta) e^2 \lambda}{4\pi\epsilon_0 m_e} dz. \quad \text{(A20)}$$

Inserting Eq. (A19) and removing the constant density term yields:

$$\Delta\phi(\zeta) = \int \frac{\omega_{\rm pe}^2 \lambda}{4\pi} \frac{\delta n_e}{n_{e0}} \sin(\omega_{\rm pe}\zeta) dz, \quad \text{(A21)}$$

with $\omega_{\rm pe}^2/n_{e0} = e^2/\epsilon_0 m_e$. Assuming that there is no significant longitudinal variation this can be integrated over the length L

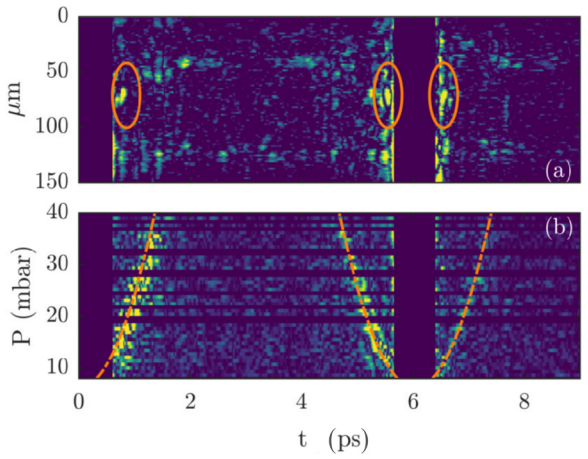

FIG. 7. (a) Intensity of the Fourier transform of the recorded spectral interferograms. The three TESS satellites on either side of the sideband at $t = \Delta\zeta = 6$ ps, and next to the DC band at $t = 0$ ps are indicated. (b) Waterfall plot of Fourier transformed interferograms for a range of cell pressures P. For each Fourier transform a 1.7 μm wide strip, centered on the peak of the satellite, is shown. The dashed line shows a parabolic fit to the satellite-to-sideband separation, using the satellites on the left side of the sideband. The above plots are shown using a logarithmic intensity scale.

of the plasma:

$$\Delta\phi(\zeta) = \frac{\omega_{\mathrm{pe}}^2\lambda}{4\pi}\frac{\delta n_e}{n_{e0}}\sin(\omega_{\mathrm{pe}}\zeta)L. \tag{A22}$$

The phase amplitude is thus identified as:

$$\phi_0 = \frac{\omega_{\mathrm{pe}}^2\lambda}{4\pi}\frac{\delta n_e}{n_{e0}}L. \tag{A23}$$

Using Eq. (A18) the relative wakefield amplitude $\delta n_e/n_{e0}$ is given by:

$$\frac{\delta n_e}{n_{e0}} = \phi_0\frac{4\pi}{\omega_{\mathrm{pe}}^2\lambda L} \tag{A24}$$

$$= \frac{2r}{\mathcal{F}(\omega_{\mathrm{pe}})}\frac{4\pi}{\omega_{\mathrm{pe}}^2\lambda L}. \tag{A25}$$

4. Pressure scan

In addition to varying the temporal delay ζ to measure the wakefield amplitude over time, in a separate experiment the pressure of hydrogen was was varied between 10 mbar and 40 mbar. A one-pixel wide slice in the y direction centered on the TESS peak was selected for each shot, and used to populate the waterfall plot in Fig. 7. The positions of the peaks relative to the sideband were then measured as a function of plasma density. This data was used to fit the expression $\tau = \varphi^{(2)}\omega_{\mathrm{pe}}$, using the GDD ($\varphi^{(2)}$) as the fitting parameter. Fitting directly to the data, a GDD value of $\varphi^{(2)} = (15203 \pm 327)\,\mathrm{fs}^2$ was obtained. However, it was observed that the data appeared to be offset from this simple fit, as can be seen in Fig. 8. This is likely caused by a drop in pressure between the location of the pressure gauge, which was connected to the gas pipe at a distance of ∼2 m from the cell. A second fit was therefore performed, where the pressure in the cell was assumed to

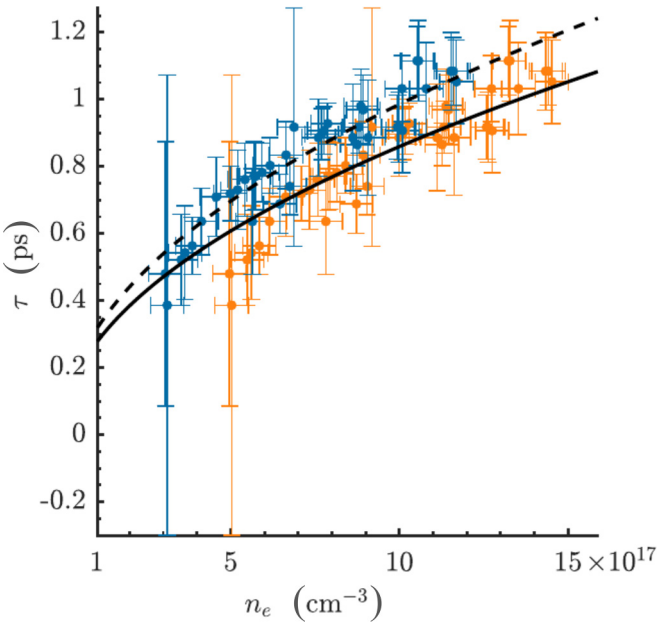

FIG. 8. Plot showing a fit to the temporal separation τ between the sideband and the TESS satellites as a function of plasma density. The red points assume that the pressure in the cell is that measured by the gauge, P_{meas}; the blue points assume that the true pressure in the cell is given by $P_{\mathrm{cell}} = \alpha P_{\mathrm{meas}} - P_0$. For both plots that the electron density is calculated assuming complete ionization of the H2 gas at the corresponding pressure. The horizontal error bars correspond to the pressure resolution of 1 mbar of the pressure gauge, and the vertical bars show the estimated error of the TESS satellite location. The solid (dashed) line shows a fit to the red (blue) points of the form $\tau = \omega_{\mathrm{pe}}\varphi^{(2)}$.

be given by: $P_{\mathrm{cell}} = \alpha(P_{\mathrm{gauge}} - P_0)$, where the offset P_0 accounts for any potential calibration offset. With this method the fitted parameters were found to be $\alpha = 0.96$, $P_0 = 3$ mbar, and $\varphi^{(2)} = (16946 \pm 81)\,\mathrm{fs}^2$, which is also shown in Fig. 8 (where the offset and shift parameters have been applied to the measured data rather than to the fit). This value of the GDD is within ∼10% of that obtained using the spectral blowout technique described in Appendix, confirming that the procedure adopted for relating the cell pressure to the gauge pressure is correct.

5. Particle-in-cell simulations

Numerical simulations of the experiments were performed with the relativistic particle-in-cell code SMILEI [38] on the ARCHER UK National Supercomputing Service and the Oxford Advanced Research Computing (ARC) Arcus-B cluster, using the same parameters as used in the experiment (the parameters used in the simulations are summarized in Table III). In the simulations, the plasma has a longitudinal and transverse extent of 240 μm ($8\lambda_p$) and 160 μm, respectively, at a uniform plasma density, $n_{e0} = 9.7\times10^{17}$ cm^{-3}. The simulation window was fixed, and boundaries were absorptive to electromagnetic radiation and reflective to electron and ion particles. The wakefield amplitude was calculated from that of the electric field of the Fourier mode corresponding to the wakefield plasma oscillation. Modulations of the longitudinal

TABLE III. Parameters of plasma, and drive and probe laser beams.

Simulation laser and plasma parameters	
Drive pulse parameters:	
Wavelength (nm)	800
Pulse duration (FWHM) (fs)	40
Pulse width (FWHM) (μm)	45
Peak intensity (Wm^{-2})	1×10^{18}
a_0	0.5
Plasma parameters:	
n_e (m^{-3})	9.7×10^{23}
λ_D (μm)	0.025
Δx (λ_D)	1
Δy (λ_D)	5
Δt (t_{CFL})	0.95
n_{ppc}	64
$x_{\max}$ (λ_p)	8
$y_{\max}$ (μm)	160

electric field developed within two picoseconds after excitation in the simulations, on a scale much smaller than the wakefield wavelength (∼1.3 μm versus $\lambda_p \approx 30$ μm).

6. Estimating the plasma temperature

In order to estimate the parameter W, which determines whether the modulational instability is in the strong- or weak-field regime, for the experimental conditions described in this paper we need an estimate of the temperature after ionization in the plasma. To obtain this estimate, we performed 2D particle-in-cell (PIC) simulations in the code Extendable PIC Open Collaboration (EPOCH) [42]. EPOCH includes ionization models, which take into account both tunneling and barrier suppression ionization pathways [42]. Collisional ionization is a third pathway that is less important in the case of short-pulse laser ionization; with a measured ionization cross section of hydrogen of $\sigma \approx 5\times10^{-17}\,\mathrm{cm}^2$ [43] for non-relativistic electrons with quiver velocities $v_{\mathrm{osc}} = a_0 c \approx 0.5c$ (with $a_0 \approx 0.5$), the ionization rate is approximately given by:

$$W = n_e \sigma v_{\mathrm{osc}}[\mathrm{s}^{-1}] \approx 0.72\,\mathrm{ps}^{-1}. \tag{A26}$$

Since collisional ionization is important over the scale of picoseconds rather than femtoseconds, as is the case for short-pulse laser ionization, we neglected this contribution in the simulations. The simulation parameters, which were chosen to be equal to the experimental parameters, are summarized in Table IV. Two different methods were used for estimating the temperature from these simulations. In the first, which is a built-in temperature probe in EPOCH, the temperature is approximated as the standard deviation of the total momentum in each simulation cell i,

$$k_b T_i \approx \frac{\langle p^2\rangle_i}{2m}. \tag{A27}$$

Averaging along the axis of laser propagation, we obtained an average on-axis temperature of 2.75 eV. The second way of approximating the temperature is by measuring the random (thermal) motion of the electrons, from which we obtained the thermal energy distribution $E_{\mathrm{thermal}} = p^2_{\mathrm{thermal}}/2m$. During the time that the drive laser spends in the plasma slab, there is a strong coherent quiver motion at the laser frequency. By filtering out this low-frequency component from the momentum we are left with only the thermal component from which we estimated the thermal energy distribution. The temperature was obtained using a fit of the Maxwell-Boltzmann distribution, with the temperature T as the fitting parameter:

$$f_E(E,T) = 2\sqrt{\frac{E}{\pi}}\left(\frac{1}{k_B T}\right)^{3/2}\exp\left(\frac{-E}{k_B T}\right). \tag{A28}$$

The laser-ionization processes investigated in this paper do not initially lead to a thermal distribution. Over time however, the electrons will equilibrate to a thermal distribution through collisions. We found that the simulation results could be well characterized as a sum of two approximately equal electron populations with different temperatures T_1 and T_2, with $T_1 = 0.26$ eV and $T_2 = 1.54$ eV. Coulomb collisions between these two populations lead to a thermal distribution after a short time. This equilibration process may be described by [44]:

$$\frac{dT_\alpha}{dt} = \sum_\beta \bar{\nu}_\epsilon^{\alpha\backslash\beta}(T_\beta - T_\alpha), \tag{A29}$$

where the Spitzer collision frequency is given by:

$$\bar{\nu}_\epsilon^{\alpha\backslash\beta} = 1.8\times10^{-19}\frac{(m_\alpha m_\beta)^{1/2}Z_\alpha^2 Z_\beta^2 n_\beta \ln\lambda}{(m_\alpha T_\beta + m_\beta T_\alpha)^{3/2}}\mathrm{s}^{-1}. \tag{A30}$$

For electron-electron equilibration $m_{\alpha,\beta} = m_e$, $Z_\alpha = Z_\beta = 1$. Since it was found that the populations were approximately equal in size, we used $n_\alpha = n_\beta = 0.5 n_e$.

The Coulomb logarithm for these parameters is $\ln\lambda \approx 13.7$. The equilibration time was defined as [44]

$$\tau_\epsilon^{\alpha/\beta} \equiv \frac{1}{\bar{\nu}_\epsilon^{\alpha\backslash\beta}} \approx 1.7\times10^5\frac{(T_\alpha[\mathrm{eV}] + T_\beta[\mathrm{eV}])^{\frac{3}{2}}}{n_\beta[\mathrm{cm}^{-3}]\ln\lambda}\mathrm{s} \approx 0.1\,\mathrm{ps}. \tag{A31}$$

With the low temperature obtained in the simulation, one sees that $\tau \ll 1$ ps. The two different plasma electron will also become isotropic on a similar timescale [45], and will therefore be fully thermalized on a timescale much shorter than the picosecond timescale relevant for the wakefield decay process. The final electron temperature used was the average between the two methods outlined in this section, $T = 2.75/2 + (0.26/2 + 1.54/2)/2 \approx 2$ eV.

TABLE IV. Simulation parameters used in 2D PIC simulations to estimate the plasma electron temperature.

Parameter	Value	Unit
Particles per cell	32	–
Simulation length	150	μm
Simulation width	300	μm
Resolution (along laser axis)	0.05	λ
Resolution (perpendicular to laser axis)	0.1	λ
Gas species	H_2	–
Plasma density	9.7×10^{17}	cm^{-3}
Laser temporal duration	48.9	fs
Laser spot width	52.3	μm
Laser intensity	6.5×10^{17}	Wcm^{-2}

[1] T. Tajima and J. M. Dawson, Laser electron accelerator, Phys. Rev. Lett. **43**, 267 (1979).

[2] W. P. Leemans, B. Nagler, A. J. Gonsalves, C. Tóth, K. Nakamura, C. G. R. Geddes, E. Esarey, C. B. Schroeder, and S. M. Hooker, GeV electron beams from a centimetre-scale accelerator, Nature Phys. **2**, 696 (2006).

[3] A. J. Gonsalves, K. Nakamura, J. Daniels, C. Benedetti, C. Pieronek, T. C. H. de Raadt, S. Steinke, J. H. Bin, S. S. Bulanov, J. van Tilborg, C. G. R. Geddes, C. B. Schroeder, C. Tóth, E. Esarey, K. Swanson, L. Fan-Chiang, G. Bagdasarov, N. Bobrova, V. Gasilov, G. Korn, P. Sasorov *et al.*, Petawatt laser guiding and electron beam acceleration to 8 GeV in a laser-heated capillary discharge waveguide, Phys. Rev. Lett. **122**, 084801 (2019).

[4] V. Yakimenko, L. Alsberg, E. Bong, G. Bouchard, C. Clarke, C. Emma, S. Green, C. Hast, M. J. Hogan, J. Seabury, N. Lipkowitz, B. O'Shea, D. Storey, G. White, and G. Yocky, FACET-II facility for advanced accelerator experimental tests, Phys. Rev. Accel. Beams **22**, 101301 (2019).

[5] R. Pompili, D. Alesini, M. P. Anania, M. Behtouei, M. Bellaveglia, A. Biagioni, F. G. Bisesto, M. Cesarini, E. Chiadroni, A. Cianchi, G. Costa, M. Croia, A. Del Dotto, D. Di Giovenale, M. Diomede, F. Dipace, M. Ferrario, A. Giribono, V. Lollo, L. Magnisi *et al.*, Energy spread minimization in a beam-driven plasma wakefield accelerator, Nature Phys. **17**, 499 (2021).

[6] E. Adli, A. Ahuja, O. Apsimon, R. Apsimon, D. Barrientos, F. Batsch, J. Bauche, M. Bernardini, T. Bohl, C. Bracco, G. Burt, A. Caldwell, M. Cascella, J. Chappell, E. Chevallay, M. Chung, D. Cooke, H. Damerau, L. Deacon, L. H. Deubner *et al.*, Acceleration of electrons in the plasma wakefield of a proton bunch, Nature (London) **561**, 363 (2018).

[7] F. Albert, N. Lemos, J. L. Shaw, B. B. Pollock, C. Goyon, W. Schumaker, A. M. Saunders, K. A. Marsh, A. Pak, J. E. Ralph, J. L. Martins, L. D. Amorim, R. W. Falcone, S. H. Glenzer, J. D. Moody, and C. Joshi, Observation of betatron x-ray radiation in a self-modulated laser wakefield accelerator driven with picosecond laser pulses, Phys. Rev. Lett. **118**, 134801 (2017).

[8] W. Wang, K. Feng, L. Ke, C. Yu, Y. Xu, R. Qi, Y. Chen, Z. Qin, Z. Zhang, M. Fang, J. Liu, K. Jiang, H. Wang, C. Wang, X. Yang, F. Wu, Y. Leng, J. Liu, R. Li, and Z. Xu, Free-electron lasing at 27 nanometres based on a laser wakefield accelerator, Nature (London) **595**, 516 (2021).

[9] R. Pompili *et al.*, Free-electron lasing with compact beam-driven plasma wakefield accelerator, Nature **605**, 659 (2022).

[10] S. M. Hooker, R. Bartolini, S. P. D. Mangles, A. Tünnermann, L. Corner, J. Limpert, A. Seryi, and R. Walczak, Multi-pulse laser wakefield acceleration: a new route to efficient, high-repetition-rate plasma accelerators and high flux radiation sources, J. Phys. B: At., Mol. Opt. Phys. **47**, 234003 (2014).

[11] J. Cowley, C. Thornton, C. Arran, R. J. Shalloo, L. Corner, G. Cheung, C. D. Gregory, S. P. D. Mangles, N. H. Matlis, D. R. Symes, R. Walczak, and S. M. Hooker, Excitation and control of plasma wakefields by multiple laser pulses, Phys. Rev. Lett. **119**, 044802 (2017).

[12] P. Muggli, B. Allen, V. E. Yakimenko, J. Park, M. Babzien, K. P. Kusche, and W. D. Kimura, Simple method for generating adjustable trains of picosecond electron bunches, Phys. Rev. Spec. Top. Accel Beams **13**, 052803 (2010).

[13] O. Jakobsson, S. M. Hooker, and R. Walczak, Gev-scale accelerators driven by plasma-modulated pulses from kilohertz lasers, Phys. Rev. Lett. **127**, 184801 (2021).

[14] A. Tünnermann, T. Schreiber, and J. Limpert, Fiber lasers and amplifiers: An ultrafast performance evolution, Appl. Opt. **49**, F71 (2010).

[15] P. Mora, D. Pesme, A. Heron, G. Laval, and N. Silvestre, Modulational instability and its consequences for the beat-wave accelerator, Phys. Rev. Lett. **61**, 1611 (1988).

[16] F. Amiranoff, M. Laberge, J. R. Marquès, F. Moulin, E. Fabre, B. Cros, G. Matthieussent, P. Benkheiri, F. Jacquet, J. Meyer, P. Miné, C. Stenz, and P. Mora, Observation of modulational instability in nd-laser beat-wave experiments, Phys. Rev. Lett. **68**, 3710 (1992).

[17] F. Amiranoff, M. Laberge, J. R. Marquès, F. Moulin, E. Fabre, B. Cros, G. Matthieussent, P. Benkheiri, F. Jacquet, J. Meyer, P. Miné, C. Stenz, and P. Mora, Observation of modulational instability in nd-laser beat-wave experiments, Phys. Rev. Lett. **69**, 996(E) (1992).

[18] F. Moulin, F. Amiranoff, M. Laberge, J. R. Marquès, B. Cros, G. Matthieussent, D. Bernard, F. Jacquet, P. Miné, A. Specka, C. Stenz, and P. Mora, Coupling between electron and ion waves in Nd-laser beat-wave experiments, Phys. Plasmas **1**, 1318 (1994).

[19] S. P. Le Blanc, M. C. Downer, R. Wagner, S. Y. Chen, A. Maksimchuk, G. Mourou, and D. Umstadter, Temporal characterization of a self-modulated laser wakefield, Phys. Rev. Lett. **77**, 5381 (1996).

[20] S. Y. Chen, M. Krishnan, A. Maksimchuk, and D. Umstadter, Excitation and damping of a self-modulated laser wakefield, Phys. Plasmas **7**, 403 (2000).

[21] A. Ting, K. Krushelnick, C. I. Moore, H. R. Burris, E. Esarey, J. Krall, and P. Sprangle, Temporal evolution of self-modulated laser wakefields measured by coherent thomson scattering, Phys. Rev. Lett. **77**, 5377 (1996).

[22] J. R. Marques, F. Dorchies, F. Amiranoff, P. Audebert, J. C. Gauthier, J. P. Geindre, A. Antonetti, J. T. M. Antonsen, P. Chessa, and P. Mora, Laser wakefield: experimental study of nonlinear radial electron oscillations, Phys. Plasmas **5**, 1162 (1998).

[23] H. Kotaki, M. Kando, T. Oketa, S. Masuda, J. K. Koga, S. Kondo, S. Kanazawa, T. Yokoyama, T. Matoba, and K. Nakajima, Direct measurement of coherent ultrahigh wakefields excited by intense ultrashort laser pulses in a gas-jet plasma, Phys. Plasmas **9**, 1392 (2002).

[24] J. W. Banks, S. Brunner, R. L. Berger, and T. M. Tran, Vlasov simulations of electron-ion collision effects on damping of electron plasma waves, Phys. Plasmas **23**, 032108 (2016).

[25] P. M. Bellan, *Fundamentals of Plasma Physics* (Cambridge University Press, New York, 2006).

[26] R. J. Shalloo, C. Arran, A. Picksley, A. von Boetticher, L. Corner, J. Holloway, G. Hine, J. Jonnerby, H. M. Milchberg, C. Thornton, R. Walczak, and S. M. Hooker, Low-density hydrodynamic optical-field-ionized plasma channels generated with an axicon lens, Phys. Rev. Accel. Beams **22**, 041302 (2019).

[27] A. Picksley, A. Alejo, J. Cowley, N. Bourgeois, L. Corner, L. Feder, J. Holloway, H. Jones, J. Jonnerby, H. M. Milchberg, L. R. Reid, A. J. Ross, R. Walczak, and S. Hooker, Guiding of high-intensity laser pulses in 100-mm-long hydrodynamic optical-field-ionized plasma channels, Phys. Rev. Accel. Beams **23**, 081303 (2020).

[28] A. Picksley, A. Alejo, R. J. Shalloo, C. Arran, A. von Boetticher, L. Corner, J. A. Holloway, J. Jonnerby, O. Jakobsson, C. Thornton, R. Walczak, and S. M. Hooker, Meter-scale conditioned hydrodynamic optical-field-ionized plasma channels, Phys. Rev. E **102**, 053201 (2020).

[29] A. Alejo, J. Cowley, A. Picksley, R. Walczak, and S. M. Hooker, Demonstration of kilohertz operation of hydrodynamic optical-field-ionized plasma channels, Phys. Rev. Accel. Beams **25**, 011301 (2022).

[30] J. Vieira, R. A. Fonseca, W. B. Mori, and L. O. Silva, Ion motion in self-modulated plasma wakefield accelerators, Phys. Rev. Lett. **109**, 145005 (2012).

[31] R. D'Arcy, J. Chappell, J. Beinortaite, S. Diederichs, G. Boyle, B. Foster, M. J. Garland, P. G. Caminal, C. A. Lindstrøm, G. Loisch, S. Schreiber, S. Schröder, R. J. Shalloo, M. Thévenet, S. Wesch, M. Wing, and J. Osterhoff, Recovery time of a plasma-wakefield accelerator, Nature (London) **603**, 58 (2022).

[32] R. W. Assmann, M. K. Weikum, and T. Akhter, Eupraxia conceptual design report (draft), Eur. Phys. J. Spec. Top. **229**, 3675 (2019).

[33] B. Cros, P. Muggli, C. Schroeder, S. Hooker, P. Piot, J. England, S. Gessner, J. Vieira, E. Gschwendtner, J.-L. Vay, and M. Peskin, Towards an advanced linear international collider, arXiv:1901.10370.

[34] W. P. Leemans, R. Duarte, E. Esarey, S. Fournier, C. G. Geddes, D. Lockhart, C. B. Schroeder, C. Toth, J. L. Vay, and S. Zimmermann, The Berkeley lab laser accelerator (BELLA): A 10 GeV laser plasma accelerator, AIP Conf. Proc. **1299**, 3 (2010).

[35] N. H. Matlis, S. Reed, S. S. Bulanov, V. Chvykov, G. Kalintchenko, T. Matsuoka, P. Rousseau, V. Yanovsky, A. Maksimchuk, S. Kalmykov, G. Shvets, and M. C. Downer, Snapshots of laser wakefields, Nature Phys. **2**, 749 (2006).

[36] N. Matlis, A. Maksimchuk, V. Yanovsky, W. Leemans, and M. Downer, Analysis of sinusoidally modulated chirped laser pulses by temporally encoded spectral shifting, Opt. Lett. **41**, 5503 (2016).

[37] C. Arran, N. H. Matlis, R. Walczak, and S. M. Hooker, Reconstructing nonlinear plasma wakefields using a generalized temporally encoded spectral shifting analysis, Phys. Rev. Accel. Beams **21**, 103501 (2018).

[38] J. Derouillat, A. Beck, F. Pérez, T. Vinci, M. Chiaramello, A. Grassi, M. Flé, G. Bouchard, I. Plotnikov, N. Aunai, J. Dargent, C. Riconda, and M. Grech, Smilei: A collaborative, open-source, multi-purpose particle-in-cell code for plasma simulation, Comput. Phys. Commun. **222**, 351 (2018).

[39] A. von Boetticher, R. Walczak, and S. M. Hooker, Modulational instability in large-amplitude linear laser wakefields, Phys. Rev. E **107**, L023201 (2023).

[40] J. R. Sanmartin, Electrostatic plasma instabilities excited by a high-frequency electric field, Phys. Fluids **13**, 1533 (1970).

[41] https://zenodo.org/deposit/7945414.

[42] T. D. Arber, K. Bennett, C. S. Brady, A. Lawrence-Douglas, M. G. Ramsay, N. J. Sircombe, P. Gillies, R. G. Evans, H. Schmitz, A. R. Bell, and C. P. Ridgers, Contemporary particle-in-cell approach to laser-plasma modelling, Plasma Phys. Controlled Fusion **57**, 113001 (2015).

[43] M. B. Shah, D. S. Elliott, and H. B. Gilbody, Pulsed crossed-beam study of the ionization of atomic hydrogen by electron impact, J. Phys. B **20**, 3501 (1987).

[44] D. B. Melrose, Plasma formulary, *Instabilities in Space and Laboratory Plasmas* (Cambridge University Press, Cambridge, 2010).

[45] L. Spitzer Jr., *Physics of Fully Ionized Gases* (Dover Publications, New York, 2006).